Amphipathic Binder Integrating Ultrathin and Highly Ion-conductive Membrane for Cell-level High Energy Density All-solid-state Batteries

*Daxian Cao[1], Qiang Li[1], Xiao Sun[1], Ying Wang[1], Xianhui Zhao[2], Ercan Cakmak[3], Wentao Liang[4], Alexander Anderson[1], Soydan Ozcan[2], Hongli Zhu[1, *]*

[1]Department of Mechanical and Industrial Engineering, Northeastern University, Boston, Massachusetts 02115, USA

[2]Chemical Sciences Division, Oak Ridge National Laboratory, Oak Ridge, TN, 37831, United States

[3]Materials Science and Technology Division, Oak Ridge National Laboratory, Oak Ridge, TN, 37831, United States

[4]Kostas Advanced Nanocharacterization Facility (KANCF), Northeastern University, Burlington, Massachusetts 01803, United States

***Corresponding author:** h.zhu@neu.edu;*

Abstract

Current sulfide solid-state electrolyte (SE) membranes utilized in all-solid-state lithium batteries (ASLBs) have a high thickness (0.5~1.0 mm) and low ion conductance (<25 mS), which limit the cell-level energy and power densities. Based on ethyl cellulose's unique amphipathic molecular structure, superior thermal stability, and excellent binding capability, this work fabricated a freestanding SE membrane with an ultralow thickness of 47 μm. With ethyl cellulose as an effective disperser and binder, the Li_6PS_5Cl is uniformly dispersed in toluene and possesses superior film formability. In addition, ultralow areal resistance of 4.32 Ω cm^{-2} and remarkable ion

conductance of 291 mS (one order higher than the conventional sulfide SE membrane) have been achieved. The ASLBs assembled with this SE membrane delivers cell-level high gravimetric and volumetric energy densities of 175 Wh kg^{-1} and 675 Wh L^{-1}, individually.

Keywords: Ion conductive membrane, Binder, All-solid-state batteries, Cell-level energy density, Sulfide electrolyte, Cathode stabilization

Introduction

Nowadays, safety issues and insufficient energy density (<250 Wh kg^{-1}) are two main concerns when applying commercial lithium-ion batteries (LiBs) to applications such as electric vehicles (EVs) and portable electronics.[1, 2] All-solid-state lithium batteries (ASLBs) coupling solid-state electrolytes (SEs) with high-energy electrodes are considered an effective solution to overcome these two challenges.[3] Most SEs, especially the ceramic types, are incombustible, naturally non-volatile, and have excellent thermal stability.[4] The employment of SEs would intrinsically address the thermal runaway caused by flammable organic liquid electrolytes in conventional LiBs. Additionally, SEs possessing a high elastic modulus were regarded to suppress the metallic anode Li metal dendrite growth.[5] The employment of Li metal can significantly boost the energy densities of the ASLBs. Furthermore, due to their solid state, SEs could enable the ASLBs a bipolar cell architecture, which would allow the cells to be stacked, further enhancing the energy densities.[6, 7] Thus, ASLBs are highly promising to achieve high safety and the desired energy densities (>500 Wh kg^{-1}, >700 Wh L^{-1}) to meet the demand of EVs.[2]

However, most reported ASLBs delivered far lower energy densities (<50 Wh kg^{-1}, <100 Wh L^{-1}) at the cell level.[8] This dramatic drop is mainly attributed to the utilization of thick electrolyte membranes. Note that the evaluation of cell-level energy density includes the masses and volumes

2

of all parts of the batteries. In a sheet-type ASLB, an ideal SE membrane should concurrently have low areal resistance, high ion conductance, low thickness, high mechanical and chemical stability, and lightweight. The state-of-the-art membrane in LiBs with liquid electrolytes has a thickness of ~20 μm. In contrast, most reported solid inorganic electrolyte membranes show much higher thickness (0.5~1.0 mm).[9] These high thicknesses not only dramatically reduce the cell-level energy density but also increase the internal resistance. Although some inorganic electrolytes, especially the sulfide SE, can exhibit room-temperature ionic conductivity σ of >1.0 mS cm^{-1}, the areal resistance R of the SE membrane is as high as 100 Ω cm^2, calculated based on $R = r * A = \frac{l}{\sigma}$, where r is the resistance, A is the area of the membrane, l is the thickness (we use 1 mm in this calculation), and σ is the conductivity. When further considering the interfacial resistance in cathode and anode, the internal resistance in ASLBs far exceeds the maximum limit of 40 Ω cm^2 proposed by Randau *et al.*[8]. Therefore, to achieve cell-level high energy density and efficiency for practical application, the SE membrane must simultaneously possess a low thickness and high ionic conductivity.[10] However, when reducing the thickness, the obtained membrane becomes brittle, which creates new challenges in both SE membrane fabrication and cell stability, like the short circuit of the ASLBs. It is challenging to fabricate a SE membrane with robust mechanical strength and a thin thickness (< 50 µm).

Embedding sulfide SEs into a template and the binder-assisted methods, including solution casting and dry film fabrication, are the two most reported processes to fabricate thin SE membranes.[6] However, the ionic conductivities of the obtained membranes are generally reduced dramatically.[11] The template method is challenged by the ionic insulation of the template and insufficient infiltration of SE, which causes interrupted ion conduction paths and cavities, resulting in lower ionic conductivity. The chosen binders are critical to the membrane's ionic conductivity

and mechanical strength for the binder-assisted methods. Considering sulfide SEs are chemically unstable in polar solvents, the binders selected would ideally be soluble in nonpolar solvents, which is difficult for most binders. Conventional binders-solvents systems, like polyvinylidene fluoride (PVDF) in N-methyl-2-pyrrolidone (NMP), sodium carboxymethyl cellulose-styrene butadiene rubber (CMC-SBR) in water, polyacrylic latex in water, are not suitable for sulfide SE membrane fabrication. Owing to the good solubility in nonpolar xylene and considerable binding effect, rubbers, like SBR, silicon rubber (SR), and nitrile butadiene rubber (NBR), have enabled the fabrication of thin membranes with low thicknesses through a slurry coating approach.[12] However, the ionic conductivities are not satisfactory (< 1 mS cm^{-1}) in these works. One of the major reasons is that the binders wrapped the ionic conductive ceramic powders and blocked the ion conduction paths. Therefore, on one side, the fraction of binder should be minimized to help the membrane maintains high ionic conductivity. On the other hand, the mechanical strength of the SE membrane will be challenging when the binder amount and the membrane thickness are greatly reduced. Thus, a strong binding between binder and sulfide SE is necessary. Therefore, developing advanced binders is important to prepare ultrathin, robust, and highly ion-conductive membranes.

In this work, for the first time, ethyl cellulose was employed as a disperser and binder during electrolyte suspension preparation and SE membrane fabrication. Cellulose is the most abundant biopolymer on the earth.[13] Ethyl cellulose is a derivative of cellulose through an etherification reaction, through which a certain amount of hydrophilic hydroxyl groups are converted into oleophilic ethyl groups.[14] The resultant ethyl cellulose shows unique properties, including excellent solubility in nonpolar organic solvents, excellent dispersing capability, outstanding film formability, and high binding strength. These properties enable ethyl cellulose in applications such

as food packaging, drug delivery, and emulsion fabrication.[14, 15] The high mechanical tensile strength of 47-72 MPa of ethyl cellulose benefits to the robustness when compositing with other materials.[16] Inspired by these merits, we utilized ethyl cellulose to prepare the thin SE membrane. As a result, a freestanding, ultrathin, robust, and highly ion-conductive sulfide SE membrane was successfully fabricated based on the argyrodite Li_6PS_5Cl electrolyte. Through a scalable vacuum filtration process, the thickness of the membrane was well controlled. In addition, we also investigated the excellent chemical and electrochemical compatibility of ethyl cellulose with both Li_6PS_5Cl and toluene. More importantly, the ethyl cellulose is discretely distributed inside the SE membrane instead of continuous wrapping, which was well defined through X-ray computed tomography (XCT). Li_3InCl_6 is used as the ion conductor in the cathode layer due to its high stability with $LiCoO_2$ and Li_6PS_5Cl. The ASLB produced by coupling this advanced SE and stabilized cathode displayed a high cell-level energy density for practical applications.

Results and Discussion

It is essential to employ a thin SE membrane in the ASLB with high energy densities. Compared to the conventional cold press method, the binder-assisted solution method can efficiently fabricate a thin SE membrane, and it is scalable. However, the binder must meet the following requirements: 1) high chemical compatibility with both ceramic ion conductors and solvent; 2) excellent thermal stability during high temperature (~200℃) treatment to remove solvent; 3) superior mechanical binding strength; 4) excellent film formability; 5) negligible adverse effects on ion conduction.

Fig. 1A illustrates the required compatibility among sulfide SE, binder, and solvent in the thin SE membrane fabrication through the solution method. As aforementioned, a nonpolar solvent is necessary to avoid the reaction with sulfide SE. The binder with oleophilic groups is suggested due to their better solubility in a nonpolar solvent. Since a uniformly dispersed slurry is crucial in

5

the thin film fabrication, a weak bonding between SE and binder, like the Van der Waals forces, will benefit the dispersion uniformity of SE in the nonpolar organic solvent. Therefore, the binder is desired with multifunction. Moreover, the thermal stability of the binder is essential in film fabrication, as illustrated in **Fig. 1B**. Because an additional heating process (temperature >200 ℃) was generally employed to thoroughly remove the solvent in the membrane, the binder would ideally have high thermal stability to maintain the structure and binding capability. The thermal degradation of binders at elevated temperatures causes cracks and defects in the membrane and ionic conductivity deterioration. In addition, the distribution of the binder effectively impacts the membrane's ionic conductivity, as depicted in **Fig. 1C**. Considering most of the binders are non-ion conductive, the binder may block the ion conduction if it completely wrapped the sulfide SE. The ideal protocol is that the ion conductor is continuous and binder is randomly distributed inside the SE membrane to guarantee continuous ion conduction paths. Therefore, it is vital to minimize the binder amount, which challenges the mechanical strength of the membrane. **Fig. 1D** describes the effect of the binding ability of the binder on the mechanical strength of the membrane. The weak binding will cause poor mechanical strength and limit the application of a thin SE membrane. A strong binding can enhance mechanical stability, especially with a low amount of binder.

Different polymers were tested and screened in this work, including regular cellulose, 2,2,6,6-tetramethylpiperidine-1-oxyl (TEMPO) oxidized cellulose nanofiber grafted with polyethylene glycol, and flax fiber, but all of them show poor dispersion and film formability when compositing with Li_6PS_5Cl (Fig. S1, S2) in toluene. In contrast, ethyl cellulose with the oleophilic ethyl groups has excellent solubility in toluene, as presented in Fig. S3. The amphipathic property (oleophilic of ethyl groups and hydrophilic of hydroxyl groups) of ethyl cellulose enables a uniform and stable dispersion of ethyl cellulose with sulfide SE in toluene like surfactant. Meanwhile, the remained

6

hydroxyl groups on ethyl cellulose form a mild bonding with sulfide SE due to the interaction of the negative hydroxyl groups with positive electron-accept sites, such as P^{5+} and Li^+. Moreover, the strong binding and excellent film formability of ethyl cellulose enable the thin membrane formation with considerable mechanical strength even at a low ratio (2 wt.%). In addition, owing to the excellent thermal stability over 200 °C (as shown in Fig. S4), ethyl cellulose could survive in the high-temperature solvent removal process. Ultimately, ethyl cellulose was selected based on its unique amphipathicity, mechanical binding strength, and excellent thermal stability. **Fig. 1E** illustrates the compatibility among Li_6PS_5Cl, ethyl cellulose, and toluene in this process. Li_6PS_5Cl is a widely studied sulfide SE due to its outstanding ionic conductivity (~1.6 mS cm^{-1}), facile synthesis, and low cost. Furthermore, Li_6PS_5Cl shows excellent stability when dispersed in toluene due to the low polarity of toluene (0.099 of relative polarity)[17], resulting in excellent compatibility and an intact ionic conductivity after treatment. Thus, the system using Li_6PS_5Cl, ethyl cellulose, and toluene enables the successful fabrication of a thin SE membrane owning high ionic conductivity and mechanical strength at the same time.

The employment of a thin SE membrane could significantly boost the energy densities of the ASLB. **Fig. 1F** displays the estimated cell-level gravimetric and volumetric energy densities (including cathode, anode, and electrolyte) as the factor of the thickness of the SE membrane in a typical sheet-type ASLB coupling $LiCoO_2$ and Li metal. The detailed information used for the estimation is listed in **Table S1**. As the SE membrane thickness varies from 1000 μm to 20 μm, both gravimetric and volumetric energy density are dramatically increased from 65 Wh kg^{-1} and 106 Wh L^{-1} to 484 Wh kg^{-1} and 1174 Wh L^{-1}, respectively. Thus, compared to the SE pellet with high thickness, the thin SE membrane contributes a lightweight and higher energy density and a reduced internal resistance resulting in enhanced energy storage efficiency in ASLBs.
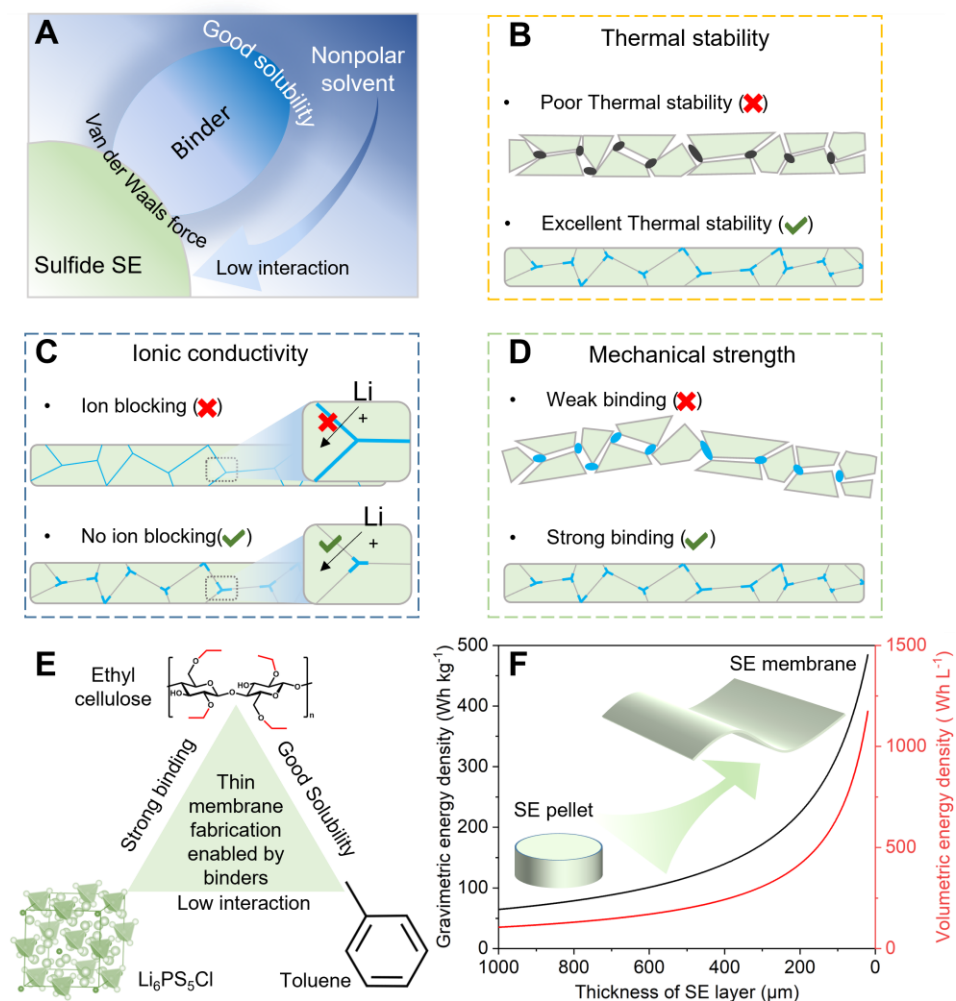
Figure 1 Overview of this work. (**A**) Illustration of compatibility among sulfide SE, binder, and solvent. Schematic to display the effect of binder on (**B**) thermal stability, (**C**) ionic conductivity, and (**D**) mechanical strength of the SE membrane. (**E**) Illustration of compatibility among Li_6PS_5Cl, ethyl cellulose, and toluene in thin membrane fabrication. (**F**) Estimated gravimetric and

volumetric energy density of ASLBs as the factor of the thickness of SE layers in ASLB coupling LiCoO$_2$ and Li metal.

The unique amphipathic molecular structure of ethyl cellulose enables the fabrication of a thin and robust membrane. **Fig. 2A** shows the dispersions of Li$_6$PS$_5$Cl in toluene with and without ethyl cellulose after standing for one hour. The Li$_6$PS$_5$Cl is uniformly dispersed in toluene with the addition of 2.0 wt.% ethyl cellulose. In contrast, there are apparent precipitations in the sample with no ethyl cellulose but only Li$_6$PS$_5$Cl. The enhanced dispersion stability is highly related to the amphipathic molecular structure of ethyl cellulose. Compared with conventional cellulose, ethyl cellulose partially substituted hydroxyl groups by ethyl groups (**Fig. 2B**). As shown in Attenuated total reflection Fourier-transform infrared spectroscopy (ATR-FTIR), cellulose had a well-defined peak centered at around 3500 cm^{-1}, attributed to its abundant hydroxyl groups. However, the peak at this wavenumber is much weaker for ethyl cellulose since the ethyl groups substituted the hydroxyl groups (degree of substitution was at 2.5). This substitution is also evidenced by the weaker peak of ethyl cellulose at 1430 cm^{-1} than cellulose, assigned to in-plane bending of -OH in the glucose unit. In the meantime, the peak at 1375 cm^{-1} assigned to -CH$_3$ bending presents for ethyl cellulose other than cellulose, attributed to the methyl end groups in the ethyl moieties of ethyl cellulose. We also found an asymmetric peak at around 2950-2850 cm^{-1} for ethyl cellulose, assigned to -CH stretching as reported.[18] The hydrophobic branches enable ethyl cellulose its outstanding solubility in toluene.

To further evaluate the dispersion uniformity and interaction of Li$_6$PS$_5$Cl with ethyl cellulose in toluene, the viscosities of cellulose, ethyl cellulose, Li$_6$PS$_5$Cl, Li$_6$PS$_5$Cl-cellulose, and Li$_6$PS$_5$Cl-ethyl cellulose, are compared in **Fig. 2C**. The dispersion of Li$_6$PS$_5$Cl-ethyl cellulose shows significantly higher viscosity than that of single components, suggesting excellent bonding exists

9

between Li_6PS_5Cl and ethyl cellulose. Ethyl cellulose owns a negative charge on the surface derived from the remaining hydroxyl groups. [19] Meanwhile, the phosphorus and Li ions in Li_6PS_5Cl act as electron acceptors to interact with ethyl cellulose and generate bonding.[20] This bonding helps the stable dispersion of Li_6PS_5Cl in toluene but is not strong enough to cause the degradation of Li_6PS_5Cl.

After preparing the well-dispersed Li_6PS_5Cl suspension, a vacuum filtration process was applied to fabricate a thin membrane, as shown in **Fig. 2D**. The obtained freestanding membrane was further cold-pressed into an ultrathin and dense layer for future use. In addition to the abovementioned bonding, ethyl cellulose also exhibits a strong binding effect with Li_6PS_5Cl enabling the SE membrane to be peeled off from the filter paper after filtration. As a result, the ion conduction paths in the thin SE membrane can remain continuous without blocks. Therefore, the thin membrane simultaneously achieves an intact ionic conductivity and considerable mechanical robustness.

Fig. 2E displays the as-prepared freestanding SE membrane. There are no cracks after the membrane being peeled off from the filter paper. In contrast to the conventional SE pellet with a diameter lower than 1.3 cm, the SE membrane owns a diameter of 44 mm. Employing a larger filtration setup can further scale up the sample size. For comparison, the sample prepared with the same process but without ethyl cellulose shows poor film formability where the membrane pulverizes after removing the solvent (**Fig. 2F**). The SE membrane can be further punched into smaller sizes without fracturing, as shown in Fig. S5, suggesting outstanding robustness. The as-punched SE membrane with a diameter of 1.27 cm also shows considerable flexibility, as shown in **Fig. 2G**, benefiting the following ASLB fabrication process. The areal weight of the SE membrane was as low as 7.9 mg cm^{-2}. **Fig. 2H** shows the conventional SE pellet prepared through

the cold press. The areal weight is as high as 158.7 mg cm^{-2}, 20 times higher loading compared to the thin SE membrane. The thickness of the SE membrane before pressing is 180 μm. After pressing at 300 MPa, the thickness decreases to 47 μm (**Fig. 2I**). In comparison, a regular SE pellet exhibits a much higher thickness of 976 μm.

Considering the SE membrane generally experiences a high pressure in ASLB, robustness under compression is necessary to avoid mechanical failure. **Fig 2J** displays the stress-strain profile of a thin SE membrane in an axial compression process. It suggests that the thin SE membrane experiences three stages: elastic deformation, plastic deformation, and densification, similar to the behavior of the porous wood sample. [21] The SE membrane does not show fracturing even at high compression stress of 80 MPa, although a high deformation is observed (90% reduction in thickness). In contrast, the thick SE pellet shows an obvious fracture point at low stress of 0.27 MPa (**Fig.2K**). Overall, the introduction of ethyl cellulose significantly improves the membrane robustness in the compression process attributing to the strong binding ability of ethyl cellulose with Li_6PS_5Cl.

The tensile strength of the thin SE membrane is also investigated, as shown in Fig. S6. The thin SE membrane shows a high tensile strength of 495 kPa and a high Young's modulus of 12.56 MPa. The excellent mechanical strength demonstrates that the thin SE membrane owns a good processibility in fabricating ASLBs.
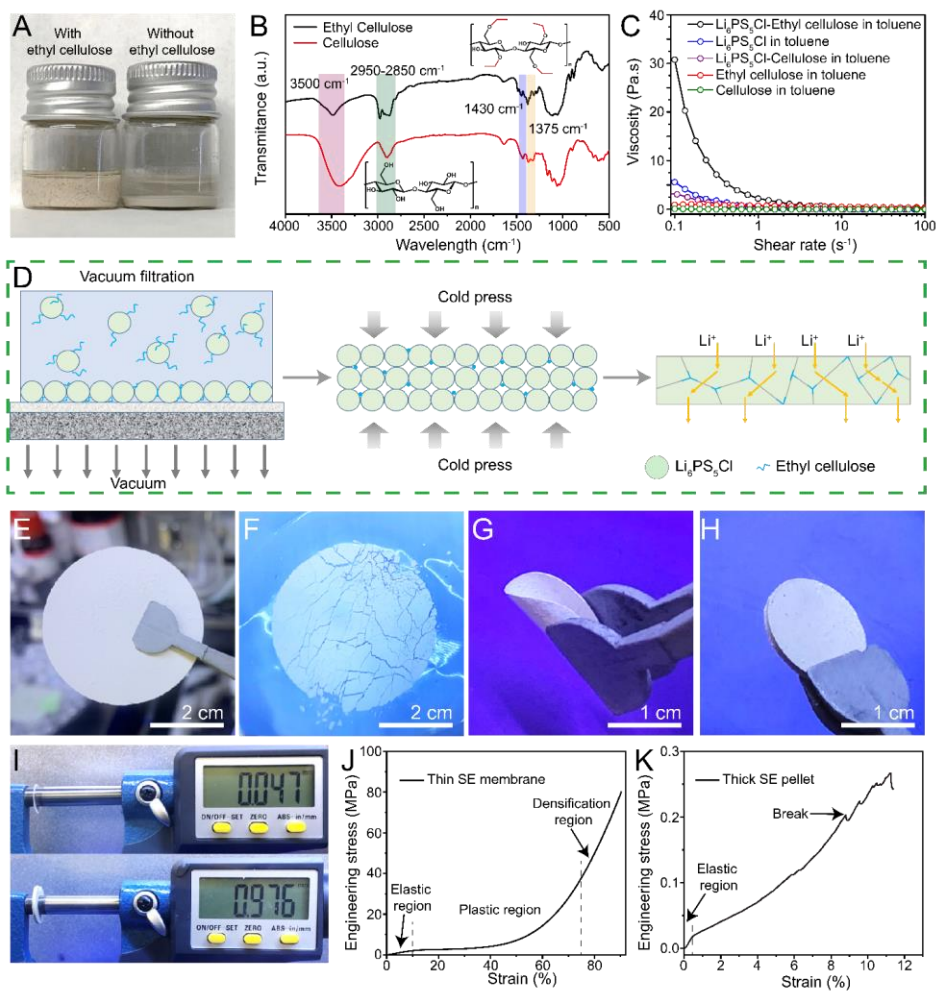
Figure 2 Fabrication of the thin SE membrane. (**A**) Photo of the Li_6PS_5Cl dispersions in toluene with/without ethyl cellulose. (**B**) FTIR spectra of ethyl cellulose and cellulose. Insets are chemical structures of ethyl cellulose and regular cellulose individually. (**C**) Viscosity as a function of the shear rate for various dispersions or solutions: Li_6PS_5Cl-ethyl cellulose in toluene, Li_6PS_5Cl in toluene, Li_6PS_5Cl-cellulose in toluene, ethyl cellulose in toluene, and cellulose in toluene. (**D**)

Schematic of the binder-assisted vacuum filtration method in fabricating the thin SE membrane. Photos of (**E**) the thin SE membrane composed of Li_6PS_5Cl and ethyl cellulose, (**F**) the thin SE membrane with only Li_6PS_5Cl, (**G**) bent thin SE membrane to show the flexibility, and (**H**) thick SE pellet. (**I**) Photos of the thin SE membrane and thick SE pellet in thickness measurement. Stress-strain profiles of (**J**) thin SE membrane and (**K**) thick SE pellet in an axial compression process.

Fig. 3A displays the cross-section scanning electron microscopy (SEM) image of the freestanding thin SE membrane. As highlighted by the yellow dash lines, the membrane shows a uniform thickness of around 50 μm, and no apparent voids or cracks are observed. The energy dispersive X-ray spectroscopy (EDS) mapping in **Fig. 3B** confirms the homogeneously distributed Cl, S, and P elements from Li_6PS_5Cl. In the magnified images in **Figs. 3C** and **3D**, the Li_6PS_5Cl particles smaller than 3 μm are closely stacked together to form a dense membrane. The ethyl cellulose is not visible on the surface or interface between Li_6PS_5Cl particles, avoiding the ion conduction block caused by the ethyl cellulose that wraps the Li_6PS_5Cl particles. **Fig. 3E** shows the top view of the membrane where there are no apparent voids or cracks. The uniform thickness and homogeneous distribution originate from the highly stable dispersion of Li_6PS_5Cl-ethyl cellulose in toluene and the efficient solvent removal in the vacuum filtration process.

As aforementioned, the Li_6PS_5Cl is highly sensitive to many polar solvents and binders. Herein the stabilities of Li_6PS_5Cl against toluene and ethyl cellulose were investigated. **Fig. 3F** compares XRD patterns of a thin SE membrane prepared with ethyl cellulose in toluene through wet filtration and a thick SE pallet without ethyl cellulose fabricated with dry pressing in the range from 20° to 80°. There are no newborn peaks and peak position shifts observed in thin SE compared with thick SE, indicating excellent compatibility between Li_6PS_5Cl with ethyl cellulose and toluene. All the

13

patterns are indexed to the typical argyrodite (cubic space group: *F*-43*m*). The prominent diffraction peaks at 25.5°, 30.0°, 31.4°, 45.0°, 47.9°, and 52.4° are indexed to (220), (311), (222), (422), (511), and (440) planes, respectively.[22] The Raman spectra of both thin SE and thick SE are displayed in **Fig. 3G** to confirm that the fabrication process has no damage to Li_6PS_5Cl. The peaks located at 195.9, 263.3, 426.7, 577.8, and 600.5 cm^{-1} are attributed to the tetrahedral PS_4^{3-} unit in argyrodite-type Li_6PS_5Cl.[23] As a result, the membrane fabrication process shows the marginal side effect on Li_6PS_5Cl, which is necessary for achieving high ionic conductivity.

The ionic conductivities of the thin SE and thick SE were evaluated through an AC impedance measurement in a symmetric cell with ion-blocking electrodes. **Fig. 3H** compares the amplified Nyquist plots of thin SE and thick SE at high and mid frequencies at 30 °C. The thin SE and thick SE thicknesses used in the measurement are 52 and 970 μm, respectively. Both SEs exhibited a typical diagram of sulfide superconductors where the plots are mainly a straight line demonstrating superior ionic conductivity. Neglecting the resistance from the external circuit, the overall ionic resistance of the SE is the sum of the bulk resistance, grain boundary resistance, and external resistance. The external resistance stemming from the outer wires and packages of the cell is measured as 1.83 Ω and subtracted in the ion conductivity evaluation (Fig. S7). Impressively, the thin SE had an ultralow resistance of 3.43 Ω and high ionic conductivity of 1.65 mS cm^{-1}, comparable to the intrinsic ionic conductivity of Li_6PS_5Cl. More importantly, the derived ion conductance is as high as 291.55 mS, representing the highest value reported so far. In contrast, the thick SE exhibits a much higher resistance of 60.37 Ω. Though the ionic conductivity is as high as 1.67 mS cm^{-1}, the ion conductance is only 16.62 mS. Therefore, a tenfold increase in ion conductance is achieved by reducing the thickness of the SE.

The ion conductions of thin and thick SEs at various temperatures (from 30 °C to 100 °C) were investigated (details in **Table S2**). The temperature affects the ionic conductivity, which is related to the activation energy of SEs. As shown in Fig. S8 and S9, the plots shift to the left at higher temperatures indicating enhanced ion conduction. **Fig. 3I** compares the temperature-dependent ion conductance of thin and thick SEs. The ion conductance of thick SE varies more than that of thin SE as temperature increased. There is an increase of over 16-fold from 16.62 to 272.48 mS in ion conductance of thick SE, attributed to an activation energy of 0.416 eV. In contrast, the thin SE delivers a slight increase in ion conductance from 291.55 mS to 1587.30 mS, resulting in activation energy of 0.264 eV. The causes of significant differences in activation energy are still under investigation. Notably, the ion conductance of thin SE at 30 °C (291.55 mS as mentioned above) is even higher than that of thick SE at 100 °C (272.48 mS), although the ionic conductivity of thin SE is much lower than that of thick SE (1.65 mS cm^{-1} at 30 °C for thin SE and 27.44 mS cm^{-1} at 100 °C for thick SE). The dramatically enhanced ion conductance was contributed to the significantly reduced thickness (from 970 μm to 50 μm) and only very slightly sacrificed ionic conductivity (from 1.67 mS cm^{-1} to 1.65 mS cm^{-1}). Moreover, the areal resistances of thin and thick SEs were evaluated to have a normalized comparison, as displayed in **Fig. 3J**. The thin SE has an ultralow areal resistance of 4.32 Ω cm^2 at 30 °C, while the thick SE exhibits a much higher value of 60.17 Ω cm^2. Excluding the charge transfer resistances, the thin SE is promising to enable the ASLB with an internal resistance lower than the demanded 40 Ω cm^2. **Fig. 3K** compares the ion conductance of SE membranes in this work with other reported values (details in **Table S3**). This thin SE membrane has the highest ion conductance among various thin-film SEs.

To further highlight the significance of ethyl cellulose, we prepared the thin film using regular cellulose as a binder through the same processes. Due to the richness in hydrophilic hydroxyl

groups, regular cellulose exhibits poor dispersion in toluene even after a mechanical pulverization. The dispersion of Li_6PS_5Cl and cellulose quickly precipitates after standing for one minute (Fig. S10). After filtration, the samples with a cellulose ratio lower than 10 wt.% showed poor film formability, attributed to the poor binding effect between cellulose and Li_6PS_5Cl. We then obtained a freestanding membrane with 10 wt.% of cellulose, and it broke into pieces when peeled off from the filter paper due to poor mechanical strength (Fig. S11). An incomplete circular membrane with a low thickness of 64 μm was fabricated after being cold pressed at 300 MPa. The ionic conductivity was only 0.12 mS cm^{-1}, which agreed well with other fiber-reinforced thin SE membranes prepared by cold pressing (Fig. S12). [24] In this sample, because of poor binding with Li_6PS_5Cl, fibrous cellulose acted as the building block but not as a binder in film fabrication. A high fraction of cellulose fibers was desired to maintain a good mechanical strength but may block the ion conduction in the membrane and reduce the ionic conductivity.
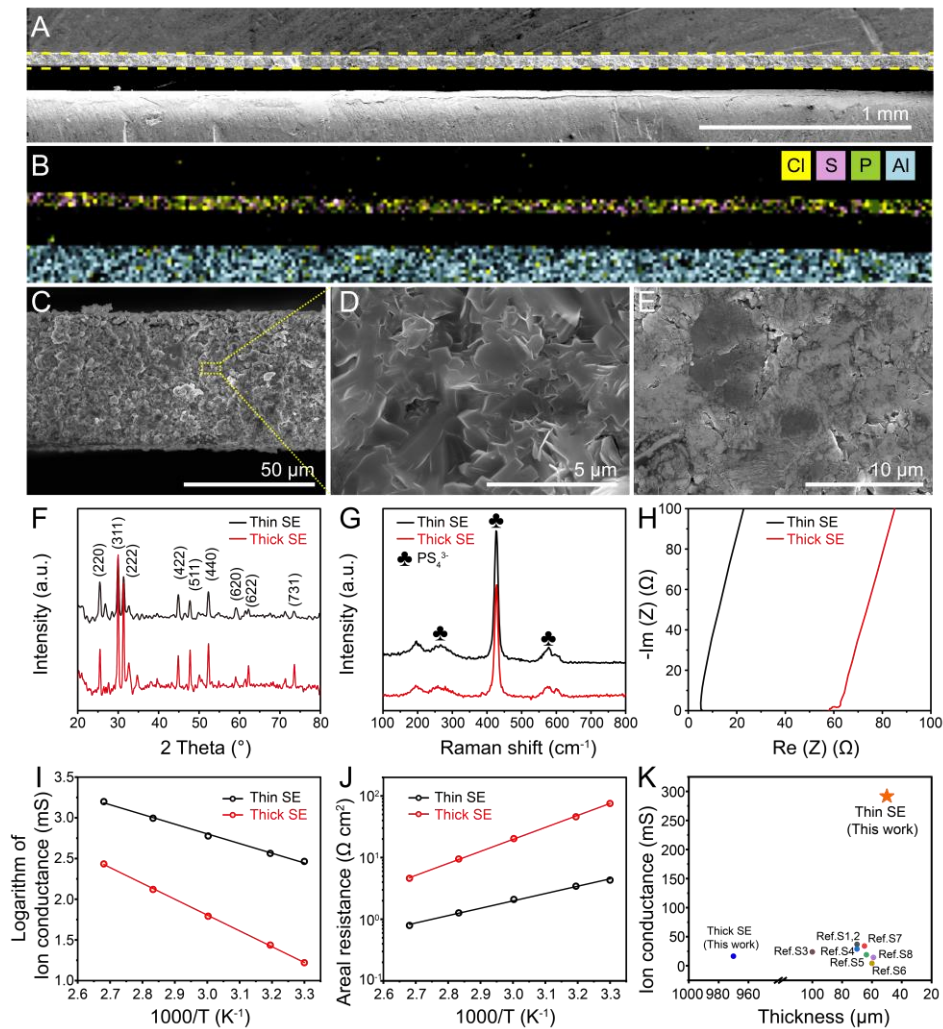
Figure 3 Performance of the thin SE membrane. (**A**) Cross-sectional SEM image and (**B**) EDS mapping of the thin SE membrane. The cross-sectional SEM images of thin SE membrane with magnitudes of (**C**) ×1k and (**D**) ×10k. (**E**) The surface morphology of the thin SE membrane from the top view. (**F**)XRD patterns and (**G**) Raman spectra of the thin and thick SEs. (**H**) Nyquist plots

in AC impedance measurement of the thin and thick SEs. The temperature-dependent (**I**) ion conductance and (**J**) areal resistances of the thin and thick SEs. (**K**) Comparison of the ion conductance at 30 °C of this SE membrane with other reported sulfide thin SE membranes.

The ion conduction pathways are significantly determined by the distributions of Li_6PS_5Cl, ethyl cellulose, and pores. Therefore, the XCT is employed to study the distribution of Li_6PS_5Cl, ethyl cellulose, and pores. Unlike SEM, which only provides surface information, XCT is a powerful technique to probe internal structure and generate three-dimensional reconstructions based on the segmental scans.[25] **Fig. 4A** shows the 2D image of the thin SE membrane from the top view. There are obvious grey level contrasts in different regions because of the density differences of the compositions. The bright region represents the Li_6PS_5Cl which is heaviest, and the dark grey region is attributed to relatively lighter ethyl cellulose, and the black spots are the pores. **Fig. 4B** highlights the distribution of Li_6PS_5Cl with yellow color. Notably, Li_6PS_5Cl takes the main fraction of the thin SE membrane and forms an integrated region, which benefits ion conduction. The regions with red color in **Fig. 4C** correspond to the ethyl cellulose which scatteringly distributes in the SE membrane and doesn't form continuous wrapping. There are also pores detected in the thin membrane, labeled as blue in **Fig. 4D**. It is interesting that pore locations are accompanied by the ethyl cellulose regions. **Fig. 4E** displays the magnified 2D image of the SE membrane. The Li_6PS_5Cl shows two different grey levels agreeing with the previous results[26]. The particle size in the bright region is much larger than that in the grey region. The loose packing of the small particles could result in a lower X-ray absorption delivering a grey color. In **Fig. 4F**, the Li_6PS_5Cl owns a high calculated volume fraction of 96.986 vol.% and shows continuous connections evidencing the high ionic conductivity. **Fig. 4G** highlights the distribution of ethyl cellulose in the SE membrane. The ethyl cellulose randomly distributes at the boundaries of Li_6PS_5Cl particles but

18

not fully wrapping the Li_6PS_5Cl particles contributing to less barrier and more continuous ion transport paths. The volume fraction of ethyl cellulose is 2.92 vol.%. In **Fig. 4H**, there are also pores observed, and the volume fraction is as low as 0.094 vol.%. The pores generation is inevitable in solid electrolyte membrane, and the porosity can reach 23% in the cold-pressed pellet using Li_6PS_5Cl powders under the pressure of 370 MPa.[27] Therefore, the addition of ethyl cellulose enables the thin SE membrane with lower pores benefiting the ion conductions. Furthermore, **Fig. 4I** displays the 3D segmented image of a 300×300×50 µm subvolume of the thin SE membrane. No huge cracks or voids are observed in the cross section. In the 3D segmented rendering of Li_6PS_5Cl (**Fig. 4J**), we can see the distribution of ion conductor in the whole membrane is continuous, which guaranteed the high ionic conductivity of the whole composite membrane. **Figure 4K** illustrates 3D segmented rendering of ethyl cellulose which exists as the point and scatteringly distributed in this subvolume. In **Fig. 4L**, there are also sporadic pores observed, demonstrating the thin SE membrane owning high density.
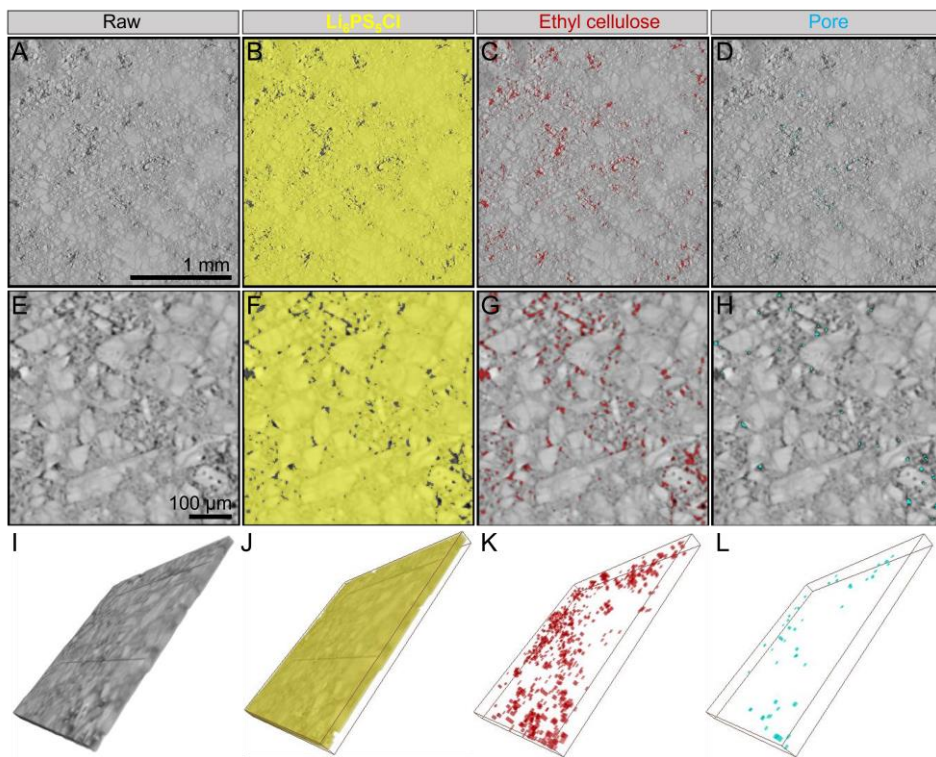
Figure 4. Distribution of Li₆PS₅Cl and ethyl cellulose in thin SE membrane revealed by X-ray computed tomography. (A) Reconstructed 2D images of the thin SE membrane in the surface and the distribution of (B) Li$_6$PS$_5$Cl labeled with yellow color, (C) ethyl cellulose marked with red color, and (D) pores tagged with blue color. (E) Magnified surface images of the thin membrane and the distribution of (F) Li$_6$PS$_5$Cl labeled with yellow color, (G) ethyl cellulose marked with red color, and (H) pores labeled with blue color. (I) 3D segmented image of a 500×500×50 µm subvolume of the thin SE membrane, and the renderings to show the distribution of (J) Li$_6$PS$_5$Cl labeled with yellow color, (K) ethyl cellulose tagged with red color, and (L) pores marked with blue color.

In ASLBs, the cathode layer plays an equally significant role with the thin SE in boosting the energy density. Generally, the cathode layer comprises active material, SEs, and other components like carbon additives and binders. Benefiting from the high working voltage (>3.9 V), impressive capacity (>200 mAh g^{-1}), and considerable electron conductivity (~10^{-5} S cm^{-1}), lithium cobalt oxide (LiCoO$_2$) has attracted numerous attentions.[28] However, sulfide SEs suffer from poor stability with LCO, resulting in an interface passivation layer formation with sluggish ion conduction, as illustrated in **Fig. 5A**. Surface coating layers, such as LiNbO$_3$ and Li$_{0.35}$La$_{0.5}$Sr$_{0.05}$TiO$_3$, have been reported to stabilize the interface between sulfide SEs and oxide cathodes. [23, 29] However, the commonly relatively low ionic conductivity (10^{-9} to 10^{-6} S cm^{-1}) of coating material rendered a new interface resistance. The high cost also constricts the large-scale application. Meanwhile, it is challenging to coat a uniform and thin layer with scalable methods for industrial application. To address this challenge, a halide superionic conductor, Li3InCl6, was employed as the SE in the cathode layer. The as-prepared Li$_3$InCl$_6$ shows an ionic conductivity of 0.4 mS cm^{-1} (Fig. S13). The Li$_3$InCl$_6$ was reported with high oxidation potential (up to 6.0 V), excellent chemical stability against LiCoO$_2$, and natural softness to achieve intimate contact with LiCoO$_2$.[30] As depicted in **Fig. 5B**, a stable interface with fast ion transfer is formed without additional interface coating. The LiCoO$_2$ - Li$_3$InCl$_6$ mixture was prepared through a facile water-mediated process. [31] **Fig. 5C** compares the XRD spectra of the LiCoO$_2$ - Li$_3$InCl$_6$ composites with that of pure LiCoO$_2$ and Li$_3$InCl$_6$. The peaks located at 19.1, 37.4, 38.4, 39.0, 45.2, and 49.5 are attributed to the (003), (101), (005), (102), (104), and (015) planes of LiCoO$_2$, respectively. The highlighted one is indexed to the (-241) plane of Li$_3$InCl$_6$. No extra peaks appear, suggesting excellent compatibility between LiCoO$_2$ and Li$_3$InCl$_6$.

In the ASLB fabrication process, the as-prepared cathode powders were further ground and pressed into the thin SE membrane. The mass loading of active material ($LiCoO_2$) is 15.9 mg cm^{-2}. The weight ratio of $LiCoO_2$ to Li_3InCl_6 is 80:20. **Fig. 5 D-I** display the cross-section SEM images and the corresponding EDS element mappings (Co, In, Cl, and S) of the pressed SE-cathode layers, respectively. The cathode layer has a thickness of 55 μm where $LiCoO_2$ particles are uniformly mixed with Li_3InCl_6.
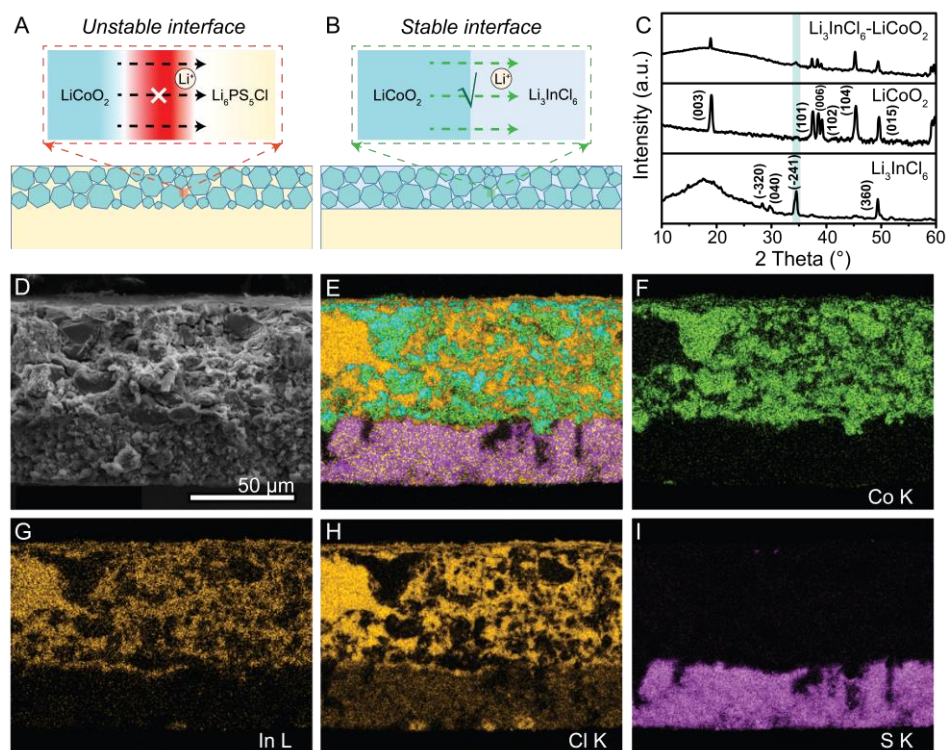

Figure 5. Stabilization of the cathode layer. Schematics to illustrate (**A**) the sluggish ion transfer at the $LiCoO_2$/Li_6PS_5Cl interface caused by the side reaction (the red region represents newborn interphase with high resistance), (**B**) the excellent compatibility at the $LiCoO_2$/Li_3InCl_6 interface

induced fast ion transfer. (**C**) XRD spectra of pure Li_3InCl_6, $LiCoO_2$, and Li_3InCl_6-$LiCoO_2$ composites. (**D**) Cross-section SEM image of the cathode-SE layers. EDS mapping of (**E**) Overall elements, (**F**) Co, (**G**) In, (**H**) Cl, (**I**) S in the cross section of the cathode-SE layers.

We further evaluated the effects of replacing sulfide with halide in the cathode layer and reducing the thickness of the SE layer in the ASLBs. As depicted in **Figs. 6 A-C**, three cells coupling $LiCoO_2$ - Li_6PS_5Cl with thick SE (cell-1), $LiCoO_2$ - Li_3InCl_6 with thick SE (cell-2), and $LiCoO_2$ - Li_3InCl_6 with thin SE (cell-3) were assembled. The mass loading of the whole cathode and active material ($LiCoO_2$) were 19.84 and 15.87 mg cm^{-2}, respectively. To avoid the side effect caused by the anode side, In-Li acted as anode material in all three cells. All three cells were tested with a constant current/constant voltage protocol between 2.0 and 4.2 V (vs. In-Li). **Fig. 6D** displays the charge/discharge profiles of three cells at the current rate of C/20. Impressively, cell-3 (using thin SE and $LiCoO_2$ - Li_3InCl_6 cathode) has the highest discharge capacity of 172 mAh g^{-1} and initial coulombic efficiency of 98.3 %. In comparison, cell-2 (using thick SE and $LiCoO_2$ - Li_3InCl_6 cathode) has a discharge capacity of 163 mAh g^{-1} and initial coulombic efficiency of 95.9 %. The enhanced cell capacity and coulombic efficiency result from the reduced internal resistance derived from the layer thickness reduction. Meanwhile, it is not surprising that cell-1 (using thick SE and $LiCoO_2$ - Li_6PS_5Cl) had the lowest capacity of 112 mAh g^{-1} and initial coulombic efficiency of 87.0 %, which was because of the side reaction between sulfide and $LiCoO_2$. **Fig. 6E** amplifies the charge profiles of three cells in the initial cycle. The charge potential in cell-2 is 55 mV lower than that of cell-1, demonstrating the enhanced stability of Li_3InCl_6 against $LiCoO_2$ compared with Li_6PS_5Cl. Moreover, there is a 20 mV lower potential in cell-3 than that of cell-2, suggesting the lower internal resistance.

23

Fig. 6F compares the rate performances of three cells. Cell-3 exhibits rate capacities of 178, 179, 165, 134, and 124 mAh g^{-1} (on average) at the current rates of C/20, C/10, C/5, C/2, and 1C, respectively (1C equals 200 mA/g). Moreover, the capacity recovers to 177 mAh g^{-1} when recharged at C/10, demonstrating an outstanding rate performance. In comparison, cell-2 delivers similar capacity at low rates but greatly reduced capacities at high rates (101 mAh g^{-1} at C/2, and 58 mAh g^{-1} at 1C). The remarkably boosted rate performance in cell-3 is attributed to the reduced internal resistance (or enhanced ion conductance) caused by thinning the SE layer. The high resistance caused by the side reaction between $LiCoO_2$ and Li_6PS_5Cl explains the poor behavior of cell-1 at a high rate (only 25 mAh g^{-1} at 1C). **Fig. 6G** shows the long-term cycling performances of cell-2 and cell-3 at the current rate of C/5. Cell-3 exhibits a remarkable initial capacity of 160 mAh g^{-1} and maintained stability for 200 cycles with a capacity retention of 82%. The coulombic efficiency is higher than 99.8%. In contrast, cell-2 shows a lower initial capacity of 147 mAh g^{-1}. The environmental temperature variation causes the regular capacity vibration in both cells. The capacity vibration in cell-3 is more moderate than in cell-2, which is following that the ionic conductance of thin SE has lower temperature dependence than that of thick SE.
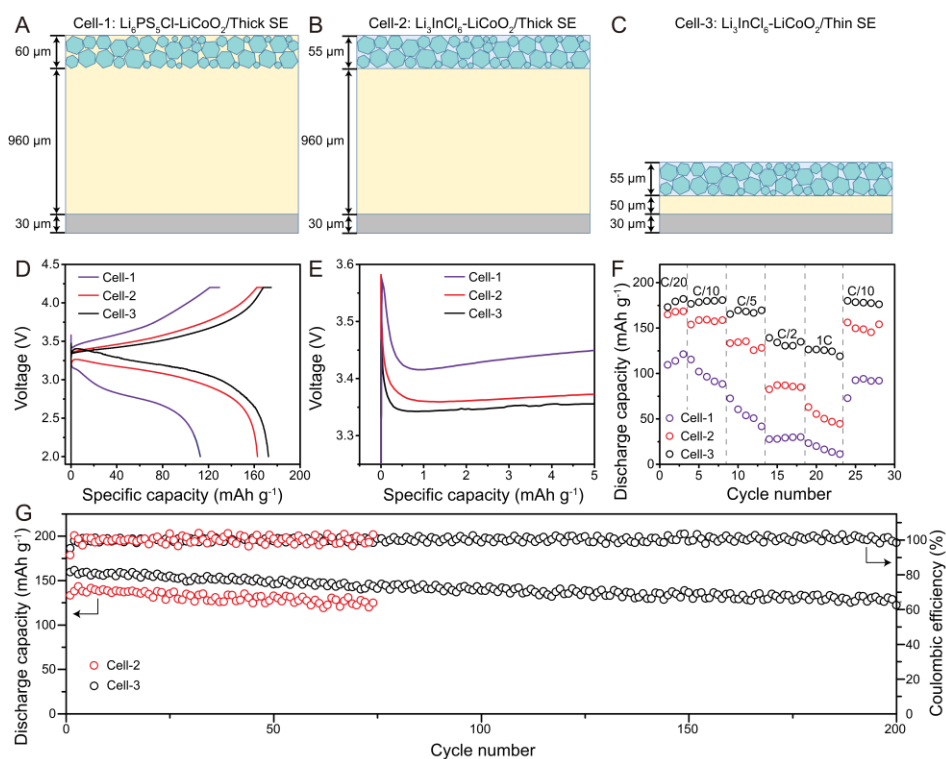
Figure 6. Performance of ASLBs. Schematics of the cell architecture of (**A**) Li_6PS_5Cl-$LiCoO_2$/thick SE, (**B**) Li_3InCl_6-$LiCoO_2$/thick SE, and (**C**) Li_3InCl_6-$LiCoO_2$/thin SE. (**D**) Charge/discharge profiles and (**E**) the amplified charge profile of three cells in the first cycle. (**F**) Rate performances of three cells. (**G**) Long-term cycling stabilities of cell 2 and cell 3 at C/5 in room temperature.

The gravimetric and volumetric energy densities of cell-3 were evaluated and compared with other reported ASLBs using $LiCoO_2$ cathode, sulfide SEs, and In (or In-Li) anode, as depicted in **Fig. 7**. The energy densities are calculated according to the weight and volume of the sum of 1) cathode, SE, and anode (E_1), and 2) only cathode and SE (E_2). E_3 is calculated as the perspective energy

densities of cell-3 when employing Li metal anode. The detailed information on the energy density calculation is listed in **Table S4** and **Table S5**. Cell-3 delivered remarkable E_1 energy densities (175 Wh kg^{-1}, 670 Wh L^{-1}) far exceeding that of other ASLBs (<30 Wh kg^{-1}, <60 Wh L^{-1}). The significant difference is highly related to replacing a thick SE pellet with a thin SE membrane. Considering that In anode is generally considered unfeasible for practical ASLBs, the E_2 energy densities that exclude the In anode weight in the calculation are discussed. As a result, cell-3 delivered an ultrahigh gravimetric energy density of 325 Wh kg^{-1} and volumetric energy density of 861 Wh L^{-1}. Furthermore, the perspective E_3 energy densities of cell-3 reach 366 Wh kg^{-1} and 795 Wh L^{-1}, respectively, attributing to the high energy density of Li metal. The critical current density (CCD) of thin SE membrane when coupled with Li metal is investigated and compared with thick SE. Fig. S14 displays the voltage profiles of these two symmetric cells during plating/stripping at a fixed capacity of 0.1 mAh cm^{-2} but a step-increased current density from 0.1 to 0.6 mA cm^{-2}. Overall, the thin SE cell delivers a critical current density of 0.5 mA cm^{-2}, the same as the thick SE cell. It demonstrates that the thickness of the SE has a limited effect on its stability with Li metal. In addition, the overpotentials in thin SE are much lower than in thick SE, evidencing the much higher ion conductance in thin SE.

26
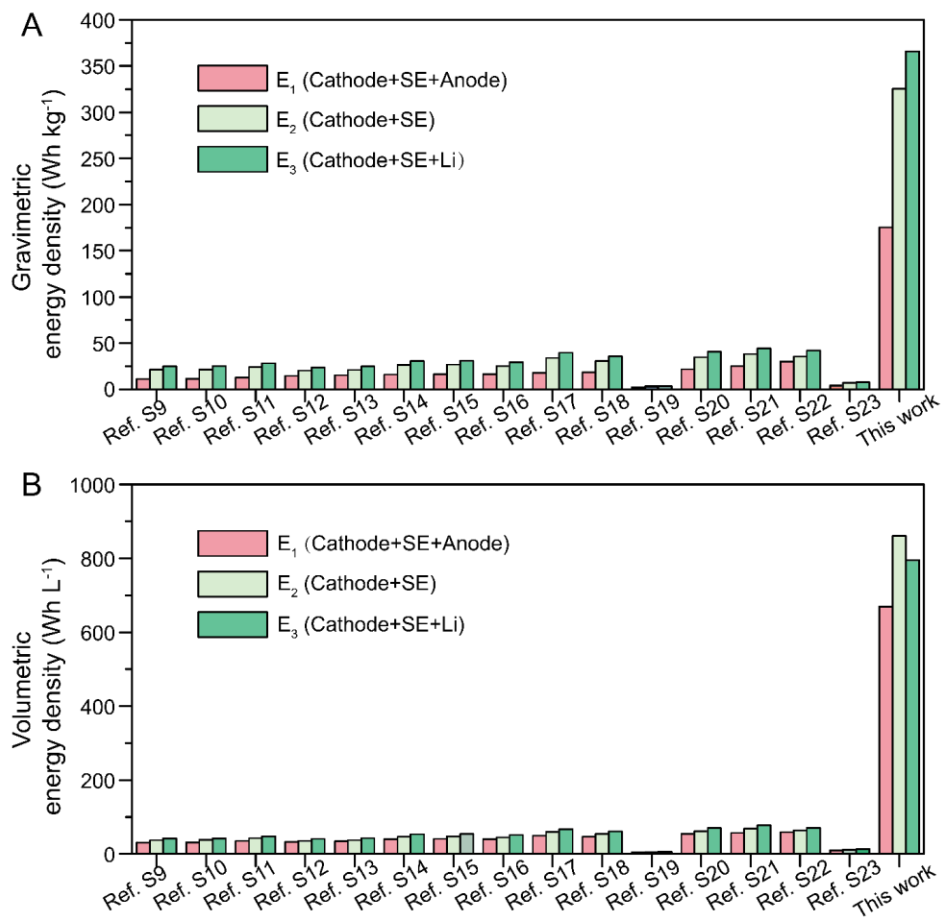
Figure 7 Energy densities evaluation. (**A**) Gravimetric and (**B**) volumetric energy densities of

Cell 3 at E_1 (cathode, SE, and anode), E_2 (cathode and SE), and E_3 (cathode, SE, and Li metal)

levels in comparison with other reported ASLBs using $LiCoO_2$ cathode, sulfide SE, and In (or In-

Li) anode.

Conclusions

The significance of developing a thin and highly ion-conductive SE membrane (thickness < 50 μm, ionic conductivity > 1.0 mS cm^{-1}) has attracted global interest in both academia and industries, but few works have achieved this number. Sulfide SEs are one of the most promising SEs to provide superior ion conductivity. However, the challenge in fabricating sulfide-based thin composite membrane is finding a binder compatible with sulfide SE and solvent simultaneously, thermally stable with high binding strength and excellent film formability. For example, nonpolar solvents are preferred for sulfide SEs to avoid the degradation of sulfide SEs, but most binders are insoluble in a nonpolar solvent. The ethyl cellulose in this work satisfies the following requirements: 1) Excellent solubility and stability in the nonpolar solvent of toluene; 2) High chemical and electrochemical stability with sulfide SE; 3) Outstanding thermal stability; 4) High binding strength; 5) Efficient dispersing capability; and (6) Excellent membrane formability. Because of the unique amphipathic molecular structure and the abovementioned merits of ethyl cellulose, we fabricated a flexible, ultrathin, and robust SE membrane through a scalable filtration method. Meanwhile, Li_3InCl_6 acted as an interfacing stabilizer and ion conductor with $LiCoO_2$ cathode, promoting the reaction kinetic and long-term cycling stability. The reported sulfide SE membrane had a low thickness of 47 μm, lightweight of 7.9 mg cm^{-2}, a superior ionic conductivity of 1.65 mS cm^{-1}, ultralow areal resistance of 4.32 Ω cm^2, ultrahigh ion conductance of 291 mS, remarkable comparison robustness under a pressure of 80 MPa, and excellent flexibility. The ASLBs employing this thin SE membrane delivered outstanding energy densities of 325 Wh kg^{-1} and 861 Wh L^{-1} based on cathode and SE layer, and cell-level energy densities of 175 Wh kg^{-1} and 670 Wh L^{-1}. This work discovered a unique binder for large-scale manufacturing of ultrathin, robust, and highly ionic conductive SE membrane for cell-level high-energy ASLBs.

Experimental section

Materials synthesis

Li₆PS₅Cl The synthesis of Li_6PS_5Cl was based on our previous work.[23] Briefly, Li_2S (Sigma-Aldrich, 99.98%), P_2S_5 (Sigma-Aldrich, 99%), and LiCl (Sigma-Aldrich, 99%) were stoichiometrically mixed through a ball milling for 10 h at 500 rpm. After that, the mixture was sealed in a glass tube and annealed at 550 °C for 6 h. The collected powder was the raw Li_6PS_5Cl. Next, the raw Li_6PS_5Cl was dispersed in toluene and experienced another ball milling process for 5 h at 400 rpm to achieve more fine particles. Finally, after a 200 °C treatment in Ar, the fine Li_6PS_5Cl powders were obtained.

Li₃InCl₆ The Li_3InCl_6 was prepared through an as-reported water-mediated approach.[32] Firstly, stoichiometric $InCl_3$ (Sigma-Aldrich, 99.999%) and LiCl (Sigma-Aldrich, 99%) were dissolved in water in sequence. The mixture was then transferred to an oven and heated at 100 °C until the most visible water was removed. After that, the collected powders were further annealed at 200 °C for 7 h in a vacuum to remove the water to get the as-prepared Li_3InCl_6.

Li₃InCl₆-LiCoO₂ The preparation of the Li_3InCl_6-$LiCoO_2$ mixture was similar to the synthesis of Li_3InCl_6, as mentioned above. The $LiCoO_2$ powders (Rogers Inc.) were added into the as-prepared solution of $InCl_3$ and LiCl in weight ratios of 80:20. Before removing the water at 100 °C in an oven, the mixture was first treated in a bath sonication for 10 min. After the same water removal processes, the Li_3InCl_6-$LiCoO_2$ mixture was transferred into the glovebox and stored for future use.

Li₆PS₅Cl-ethyl cellulose membrane **fabrication**

A vacuum filtration method was employed to prepare the thin membranes, conducted in the glovebox. Briefly, 2 mg of ethyl cellulose was first dissolved in 1 mL of toluene. After that, 98 mg of fine Li_6PS_5Cl powders were added to the ethyl cellulose solution, accompanied by continuous mechanical stirring to achieve uniform dispersion. The dispersion was then cast in the vacuum filtration system. A freestanding thin membrane can be obtained after peeling it off from the filter paper. The membrane was then sandwiched between two glass slides and heated at 150 °C for 12 h on a hot plate to remove the toluene completely. A commercial separator (Celgard 2400) was utilized as the filter paper due to limited pore size (43 nm). A coarse-frit glass filter (Fisher Scientific) with a diameter of 47 mm was used in the filtration process.

Materials Characterization

The X-ray diffraction (XRD) was conducted on PANalytical/Philips X'Pert Pro (PANalytical, Netherlands) with Cu Kα radiation. The Raman spectra were measured on a Thermo Scientific DXR (Thermo Scientific, USA) with 532 nm laser excitation. The samples are sealed with Kapton tape to avoid exposure to air. The scanning electron microscopy (SEM) and energy dispersive X-ray spectroscopy (EDS) were characterized by SEM JEOL JSM 7000F (JEOL Ltd., JAPAN). The FTIR was measured on JASCO FT/IR-6600 (JASCO International Co., Ltd., USA). The viscosity was performed on Discovery Hybrid Rheometer HR 30 (TA Instruments, US). The concentration of cellulose, ethyl cellulose, Li_6PS_5Cl, Li_6PS_5Cl-cellulose, and Li_6PS_5Cl-ethyl cellulose are 2, 2, 100, 98/2, and 98/2 mg mL^{-1} in toluene, respectively. The Compression strength was conducted on a Zwick/Roell material testing machine (ZwickRoell, USA). The thin SE membrane was cut into a circular shape with a diameter of 1/2 inch and a thickness of 0.05 mm. The thick SE pellet with the same diameter but thickness of 1 mm was prepared through a cold-press method. The displacement speed was 0.001 mm s-1. The tensile strength test was carried out in HR 30

Discovery Hybrid Rheometer-Dynamic Mechanical Analysis (DMA) (TA Instruments, US). The thin SE membrane was cut into a rectangle with 3 cm in length, 4.6 mm in width, and 0.1 mm in thickness. The displacement speed was 0.01 mm s^{-1}.

X-ray computed tomography

For the XCT measurement, a Zeiss Xradia Versa 520 XCT unit was used; operated at 30 kV and 68 µA. For increased magnification and resolution, a 4× scintillator objective was used in front of the CCD camera. A 2×2 binning (on the detector) was used for optimized measurement time and resolution; resulting in a x=y=z=2.46 µm Pixel size. XCT data was collected over a sample rotation of ω=360° with 1601 projections at equal steps. For image processing and segmentation, the ORS Dragonfly PRO v.3.5 software was used.

Electrochemical characterization

Ionic conductivity measurement

The ionic conductivities of Li_6PS_5Cl powder, Li_6PS_5Cl-ethyl cellulose membrane, and Li_3InCl_6 powder were measured using EIS by symmetric systems with different ion-blocking electrodes. The ionic conductivity measurement of Li_6PS_5Cl powder can be found in our previous work. [23] The Li_6PS_5Cl-ethyl cellulose membrane was first cut into a 12.7 mm circular sheet and then pressed under 300 MPa in a 12.7 mm PEEK die. Two pieces of indium foils (30 μm in thickness, 11.1 mm in diameter) were pressed onto two stainless steel plugs and then attached on both sides of the Li_6PS_5Cl-ethyl cellulose membrane in the die under 10 MPa. The total die with plugs was fixed in a stainless steel framework to conduct EIS directly. The ionic conductivity of Li_3InCl_6 was measured under similar processes with Li_6PS_5Cl except using stainless steel foil as electrodes to avoid the side reaction between Indium and Li_3InCl_6.

Fabrication of ASLB using thick SE

The ASLB fabrication with thick SE was conducted in the glovebox. First, 200 mg of Li_6PS_5Cl powders were pressed in a PEEK die with a diameter of 12.7 mm under 300 MPa. Then 25 mg of as-prepared Li_3InCl_6-$LiCoO_2$ mixture was casted and then pressed on one side of the Li_6PS_5Cl under 100 MPa. A piece of In-Li was pressed on the other side with a pressure of 100 MPa to work as an anode. The Cu and stainless steel foil were selected as current collectors for anode and cathode, respectively. Finally, extra pressure of 50 MPa was applied to the cell and maintained with a stainless steel framework.

Fabrication of ASLB using thin SE

The fabrication of ASLB using thin SE was similar to the fabrication of thick SE as aforementioned. A piece of In-Li foil was first pressed on the stainless steel plug with a diameter of 12.6 mm under a pressure of 300 MPa. After that, a 12.7 mm circular thin SE membrane was pressed on the In-Li foil in a PEEK die under 300 MPa. Then 25 mg of Li_3InCl_6-$LiCoO_2$ was cast on the top of thin SE and further pressed under 100 MPa. Finally, an extra pressure of 50 MPa was applied to the cell and maintained with a stainless steel framework.

Rate and cycling performance

The rate and cycling measurement were conducted with a protocol that the cell was charged at constant current to 4.2 V, held at 4.2 V for 1 h, and then discharged to 2.5 V at a constant current. The current was calculated based on the mass and capacity of cathode active material. The rate performance was measured at C/20 for the first three cycles, then C/10, C/5, C/2, 1C for five cycles, respectively, and finally recovered to C/20 for another five cycles. Long-term cycling was conducted at C/5. Here 1C means 200 mA/g based on the weight of cathode active material.

Author Contributions

D.C. and H.Z. conceived the idea. D.C., Q.L., and X.S. carried out the main experiments. X.S. provided characterization via SEM. Y.W. provided characterization via FTIR and viscosity. H.Z., D.C., and Q.L. collectively wrote the paper. Y.Z. revised the manuscript. All authors commented on the final manuscript.

Acknowledgments

Conflicts of Interest

The authors declare no conflict of interest.

References

[1]   a) X. Feng, M. Ouyang, X. Liu, L. Lu, Y. Xia, X. He, Energy Storage Materials 2018, 10, 246; b) D. Zhou, Y.-B. He, R. Liu, M. Liu, H. Du, B. Li, Q. Cai, Q.-H. Yang, F. Kang, Advanced Energy Materials 2015, 5, 1500353.
[2]   Z. P. Cano, D. Banham, S. Ye, A. Hintennach, J. Lu, M. Fowler, Z. Chen, Nature Energy 2018, 3, 279.
[3]   Q. Zhang, D. Cao, Y. Ma, A. Natan, P. Aurora, H. Zhu, Adv. Mater. 2019, 31, 1970311.
[4]   K. J. Kim, M. Balaish, M. Wadaguchi, L. Kong, J. L. M. Rupp, Advanced Energy Materials, 2021, 11, 2002689.
[5]   D. Cao, X. Sun, Q. Li, A. Natan, P. Xiang, H. Zhu, Matter 2020.
[6]   D. Cao, Y. Zhao, X. Sun, A. Natan, Y. Wang, P. Xiang, W. Wang, H. Zhu, ACS Energy Letters 2020, 3468.
[7]   J. Schnell, T. Günther, T. Knoche, C. Vieider, L. Köhler, A. Just, M. Keller, S. Passerini, G. Reinhart, Journal of Power Sources 2018, 382, 160.
[8]   S. Randau, D. A. Weber, O. Kötz, R. Koerver, P. Braun, A. Weber, E. Ivers-Tiffée, T. Adermann, J. Kulisch, W. G. Zeier, F. H. Richter, J. Janek, Nature Energy 2020, 5, 259.
[9]   J. Wu, L. Yuan, W. Zhang, Z. Li, X. Xie, Y. Huang, Energy & Environmental Science 2020.

[10]   a) Y.-G. Lee, S. Fujiki, C. Jung, N. Suzuki, N. Yashiro, R. Omoda, D.-S. Ko, T. Shiratsuchi, T. Sugimoto, S. Ryu, J. H. Ku, T. Watanabe, Y. Park, Y. Aihara, D. Im, I. T. Han, Nature Energy 2020, 5, 299; b) W. Ping, C. Wang, R. Wang, Q. Dong, Z. Lin, A. H. Brozena, J. Dai, J. Luo, L. Hu, Science Advances 2020, 6, eabc8641.

[11]   D. H. Kim, Y.-H. Lee, Y. B. Song, H. Kwak, S.-Y. Lee, Y. S. Jung, ACS Energy Letters 2020, 5, 718.

[12]   a) Y. J. Nam, D. Y. Oh, S. H. Jung, Y. S. Jung, Journal of Power Sources 2018, 375, 93; b) D. Y. Oh, Y. J. Nam, K. H. Park, S. H. Jung, K. T. Kim, A. R. Ha, Y. S. Jung, Advanced Energy Materials 2019, 9, 1802927.

[13]   H. Zhu, W. Luo, P. N. Ciesielski, Z. Fang, J. Y. Zhu, G. Henriksson, M. E. Himmel, L. Hu, Chemical Reviews 2016, 116, 9305.

[14]   G. S. Rekhi, S. S. Jambhekar, Drug Dev. Ind. Pharm. 1995, 21, 61.

[15]   P. Ahmadi, A. Jahanban-Esfahlan, A. Ahmadi, M. Tabibiazar, M. Mohammadifar, Food Reviews International 2020, 1.

[16]   L. W. McKeen, in *Film Properties of Plastics and Elastomers (Third Edition)*, (Ed: L. W. McKeen), William Andrew Publishing, Boston 2012, 353.

[17]   R. Giernoth, in *Solvents and Solvent Effects in Organic Chemistry*, 2010, 509.

[18]   V. Hospodarova, E. Singovszka, N. Stevulova, American Journal of Analytical Chemistry 2018, 9, 303.

[19]   X. Wu, L. Zhang, X. Zhang, Y. Zhu, Y. Wu, Y. Li, B. Li, S. Liu, J. Zhao, Z. Ma, Scientific Reports 2017, 7, 12079.

[20]   F. J. Simon, M. Hanauer, F. H. Richter, J. Janek, ACS Applied Materials & Interfaces 2020, 12, 11713.

[21]   Y. E. Aimene, J. A. Nairn, Wood Science and Technology 2015, 49, 21.

[22]   M. Xuan, W. Xiao, H. Xu, Y. Shen, Z. Li, S. Zhang, Z. Wang, G. Shao, Journal of Materials Chemistry A 2018, 6, 19231.

[23]   D. Cao, Y. Zhang, A. M. Nolan, X. Sun, C. Liu, J. Sheng, Y. Mo, Y. Wang, H. Zhu, Nano Lett. 2019, 20, 1483.

[24]   T. Yersak, J. R. Salvador, R. D. Schmidt, M. Cai, ACS Applied Energy Materials 2019, 2, 3523.

[25]   J. A. Lewis, F. J. Q. Cortes, Y. Liu, J. C. Miers, A. Verma, B. S. Vishnugopi, J. Tippens, D. Prakash, T. S. Marchese, S. Y. Han, C. Lee, P. P. Shetty, H.-W. Lee, P. Shevchenko, F. De Carlo, C. Saldana, P. P. Mukherjee, M. T. McDowell, Nature Materials 2021, 20, 503.

[26]   Z. Ning, D. S. Jolly, G. Li, R. De Meyere, S. D. Pu, Y. Chen, J. Kasemchainan, J. Ihli, C. Gong, B. Liu, D. L. R. Melvin, A. Bonnin, O. Magdysyuk, P. Adamson, G. O. Hartley, C. W. Monroe, T. J. Marrow, P. G. Bruce, Nature Materials 2021.

[27]   J.-M. Doux, Y. Yang, D. H. S. Tan, H. Nguyen, E. A. Wu, X. Wang, A. Banerjee, Y. S. Meng, Journal of Materials Chemistry A 2020, 8, 5049.

[28]   L. Wang, B. Chen, J. Ma, G. Cui, L. Chen, Chem. Soc. Rev. 2018, 47, 6505.

[29]   N. Ohta, K. Takada, L. Zhang, R. Ma, M. Osada, T. Sasaki, Advanced Materials 2006, 18, 2226.

[30]   X. Li, J. Liang, X. Yang, K. R. Adair, C. Wang, F. Zhao, X. Sun, Energy & Environmental Science 2020, 13, 1429.

[31]   C. Wang, J. Liang, M. Jiang, X. Li, S. Mukherjee, K. Adair, M. Zheng, Y. Zhao, F. Zhao, S. Zhang, R. Li, H. Huang, S. Zhao, L. Zhang, S. Lu, C. V. Singh, X. Sun, Nano Energy 2020, 76, 105015.

[32]   X. Li, J. Liang, N. Chen, J. Luo, K. R. Adair, C. Wang, M. N. Banis, T.-K. Sham, L. Zhang, S. Zhao, S. Lu, H. Huang, R. Li, X. Sun, Angewandte Chemie (International ed. in English) 2019, 58, 16427.